PROCEEDINGS, 49th Workshop on Geothermal Reservoir Engineering
Stanford University, Stanford, California, February 12-14, 2024
SGP-TR-227

WHOLESCALE modeling of hydro-mechanical processes at San Emidio, Nevada, U.S. on time scales of days

Xi Luo (1), Chris Sherman (2), Kurt L. Feigl (1), John Murphy (3), John Akerley (3), Hiroki Sone (1), Michael A. Cardiff (1), Jesse Hampton (1), Hao Guo (1), Neal E. Lord (1), Peter E. Sobol (1), Clifford H. Thurber (1), and Herbert F. Wang (1)

(1) University of Wisconsin-Madison, Madison, WI, United States;
(2) Lawrence Livermore National Laboratory, Livermore, CA, United States;
(3) Ormat Technologies Inc., Reno, NV, United States;

xluo245@wisc.edu

ABSTRACT

The WHOLESCALE acronym stands for Water & Hole Observations Leverage Effective Stress Calculations and Lessen Expenses. The goal of the WHOLESCALE project is to simulate the spatial distribution and temporal evolution of stress in the geothermal system at San Emidio in Nevada, United States.

The WHOLESCALE team is taking advantage of the perturbations created by changes in pumping operations during planned shutdowns in 2016, 2021, and 2022 to infer temporal changes in the state of stress in the geothermal system. This rheological experiment is based on the key idea that increasing pore-fluid pressure reduces the effective normal stress acting across preexisting faults.

We are developing a fully coupled, hydro-mechanical ("H-M") numerical model to describe seismic observations during the shutdowns using the open-source GEOS code developed at Lawrence Livermore National Laboratory. To construct the model configuration and set values for the material properties, we build on a 3-dimensional geologic and structural model of the reservoir that was updated in 2022 from earlier studies. To constrain the modeled values of permeability, we build on a sensitivity analysis of 3-dimensional hydrologic models of the San Emidio reservoir during transient events such as plant flow tests and temporary, planned shutdowns.

To specify the initial conditions and boundary conditions for the mechanical simulation, we use several indicators of stress. The fluid-flow boundary conditions for the models are driven by flow rates recorded at production and injection wells.

In refining the models, we consider two different time scales. In this paper, we focus on short time scales on the order of minutes to days. In a companion paper (Feigl et al., this meeting), we consider long time scales of the order of years.

To validate the modeling, we consider microseismic events recorded over ten days in December 2016 by a seismic array deployed before, during, and after a planned shutdown in December 2016

In this paper, we provide a snapshot of work in progress.

Keywords: WHOLESCALE, San Emidio, EGS, GPS, INSAR, FEM

INTRODUCTION

The San Emidio geothermal area is located ~100 km north of Reno Nevada in the northwestern Basin and Range province, as described previously (Matlick, 1995; Rhodes et al., 2010; Warren, 2010; Eneva et al., 2011; Moeck, 2011; Rhodes, 2011; Rhodes et al., 2011; Faulds, 2014; UNR, 2014; Teplow and Warren, 2015; Pulliam et al., 2019; Reinisch et al., 2019; Warren et al., 2019a; Feigl et al., 2020; Folsom et al., 2020; Folsom et al., 2021; Feigl et al., 2022b; Guo et al., 2022; Jahnke, 2022; Jahnke et al., 2022; Akerley et al., 2023; Jahnke et al., 2023; Sone et al., 2023).

Understanding subsurface stress can aid the development, drilling, and operational phases of geothermal operations. In this paper, we focus on the temporal changes in stress manifested as seismicity. Operators need a methodology to predict how these changes occur in time and space to manage the resource over the long term. The state of stress changes as a highly nonlinear response to multiple physical processes that can only be tracked by modern computational analysis. Accordingly, our methodology is an integrated geophysical and numerical approach for predicting the stress in a geothermal system. In short, "if we can model it, we can manage it".

As we have discussed previously (Feigl et al., 2023), anthropogenic perturbations to hydrological systems can alter the state of stress sufficiently to trigger seismic slip on pre-existing faults (e.g., Raleigh et al., 1976; Ellsworth, 2013; Segall and Lu, 2015). Similarly, extracting and injecting brine out of and into geothermal fields can also induce seismicity, especially in enhanced geothermal systems (EGS) (Majer et al., 2007; Brodsky and Lajoie, 2013; NRC, 2013; Kwiatek et al., 2015; McGarr et al., 2015; Trugman et al., 2016; Andrés et al., 2019). Such induced seismicity is caused by changes to the state of stress in and around the geothermal reservoir. Indeed, we hypothesize that increasing pore-fluid pressure reduces the effective normal stress acting across preexisting faults and induces microseismic events (MSEs).

By analyzing the data streams at geothermal fields, we can take advantage of the perturbations created by pumping operations to infer temporal changes in the state of stress in the geothermal system. For example, the PoroTomo experiment was conducted at the geothermal field at Brady Hot Springs, Nevada (Feigl and Parker, 2019). There, a scheduled cessation of both production and injection pumping produced fluid pressure changes as large as 150 kPa (roughly equivalent to 15 m of water) (Patterson et al., 2017) that are associated with microseismic events with magnitude less than M 2 (Cardiff et al., 2018) At Brady, these authors observed that "shutdowns in pumping for plant maintenance correlate with increased microseismicity" (Cardiff et al., 2018). Following these authors, we hypothesize that "extraction of fluids inhibits fault slip by increasing the effective [normal] stress on faults; in contrast, brief pumping cessations represent times when effective [normal] stress is decreased below its long-term average, increasing the likelihood of microseismicity" (Cardiff et al., 2018).

Similar phenomena have been observed at San Emidio. In the month of December 2016, more than 100 discrete microseismic events were detected as the power plant, production wells, and injection wells were shut down for maintenance (Warren et al., 2018; Warren et al., 2019a; Warren et al., 2019b). A seismic array of ~1,300 vertical-component seismic stations operated by Microseismic Inc. recorded for about a week (Warren et al., 2019a). The metadata and data are publicly available at the Geothermal Data Repository (Lord, 2016; Lord et al., 2022).

Guo et al. (2023) have analyzed the seismic data to estimate precise hypocentral locations, magnitude, and focal mechanisms. These microseismic events are small in magnitude. Although they can be detected by sensitive seismic instruments, they were not — and cannot be — felt by humans. Recent work indicates that the discrete events detected in December 2016 have a maximum (coda) magnitude M_c less than zero (Guo et al., 2023).

At San Emidio, the location and timing of the events in December 2016 are consistent with time-dependent 3-dimensional numerical models that show increased fluid pressure over length scales of the order of several kilometers from the production wells and temporal scales of the order of tens of hours from the cessation of production and injection, as described previously (Cardiff et al., 2023). Those models accounted only for hydraulic effects to simulate changes in fluid pressure. In this paper, we develop a multi-physics model that couples hydrological and mechanical (H-M) processes over time scales of hours to days. The goal is to simulate the occurrence of microseismic events observed during the shutdowns.

DATA

We are developing a fully coupled, hydro-mechanical ("H-M") numerical model using the open-source GEOS code developed at Lawrence Livermore National Laboratory (e.g., Settgast et al., 2018). To constrain the modeling effort, the WHOLESCALE team is analyzing multiple types of observational data from San Emidio.

The geometry of the GEOS model configuration is based on a 3-dimensional geologic and structural model of San Emidio that was updated in 2022 by Matt Folsom, following an exhaustive review and re-interpretation of well cuttings and logs. The new geologic model is an update from that presented earlier (Folsom et al., 2020). The 2022 version of the geologic model follows a stratigraphic column with geologic units consistent with those mapped in the field (Rhodes et al., 2010; Rhodes, 2011; Rhodes et al., 2011). The new model recognizes a pronounced north-striking outflow path, coincident with acid sulfate alteration and pervasive silicification of sediments. This rock unit (named Qas) is channelized within beach-deposits, bar gravels and other permeable strata deposited along the shoreline of ancestral lakes in the basin. The zone is marked by a sharp gravity anomaly attributed to the densification of these sediments. Other additions to the model include updated fault geometries and inclusion of a Tertiary claystone unit that marks the bottom of the alluvium in the field. Figure 5 shows a representative cross section of the geologic model. The horizontal coordinates of the mesh are specified in easting and northing in meters in Zone 11 of the Universal Transverse Mercator (UTM) projection in WGS84. The vertical coordinate is elevation (reckoned positive upwards) with respect to mean sea level, i.e. the geoid. This coordinate system (E, N, H) is right-handed.

We have converted the geologic model into a finite-element mesh that conforms to the geometry of the key faults and geologic units using a semi-automatic procedure using CUBIT (Blacker et al., 2016). For simplicity, we translate the UTM coordinates into a local coordinate system (X, Y, Z) = (E, N, H) — (286924.277, 4457966.689, 0.0) [m]. The resulting mesh is a volume with a (N-S) length ~11 km, (E-W) width ~10 km, and thickness ~3.5 km that contains 928,305 tetrahedral elements.

To assign values for the material properties of density, bulk modulus, and shear modulus in the GEOS configuration, we considered values from the geologic model as well as laboratory testing of samples collected from outcrops in the field and cuttings collected while drilling (Folsom et al., 2020; Kleich, 2022; Sone et al., 2023). The structure of these material properties is broadly consistent with that of P-wave velocity inferred from seismic tomography (Guo et al., 2023) and electric resistivity inferred from magnetotelluric surveys (Folsom et al., 2020), as shown in Figure 6. To constrain the modeled values of permeability, we build on a sensitivity analysis of 3-dimensional hydrologic models of the San Emidio reservoir during transient events such as plant flow tests and temporary, planned shutdowns (Cardiff et al., 2023a; Cardiff et al., 2023b). The material properties are listed in Figure 1.

METHODS

To define the initial conditions in terms of stress, we consider stress indicators including focal mechanisms from regional earthquakes, slickenlines on exposed fracture surfaces, wellbore stress indicators observed in the surrounding region, and secular strain rate measurements, as described previously (Jahnke et al., 2023). To define the "pre-stress" conditions, we follow the procedure outlined previously (Jahnke et al., 2023). To set the initial conditions in hydraulic pressure, we use the values calculated previously (Cardiff et al., 2023a).

To constrain the far-field boundary conditions, we consider regional indicators of stress (Jahnke et al., 2023). The vertical faces of the model domain are "rollers" to allow vertical displacement but horizontal traction. The upper surface of the problem domain is free to move, while the bottom surface is fixed. No fluid flow is allowed on any external face of the model domain. The boundary conditions are listed in Figure 2.

The flow rates of fluids into and out of the injection and production wells have been recorded by the operator. Assuming a constant temperature for the injected fluids that is lower than that of the produced fluids, we convert the volumetric flow rates into mass fluxes. In the model, the mass fluxes are imposed as sources and sinks in the perforated intervals of the modeled borehole trajectories for the injection and production wells, respectively. We assume that the wellbores follow vertical trajectories. In this H-M model, we neglect thermal effects.

Using the geometric mesh, material properties, initial conditions, boundary conditions, ran the GEOS code over a 2-day simulation period from 2016/12/08 08:11 UTC to 2016/12/10 08:13 UTC. The plant shutdown that began at 2016-12-08 19:33 UTC is included. The incremental time interval of simulation is every 60 seconds and the results are exported every 60 seconds as HDF5 files and every 10 min as VTK/VTU files. GEOS calculates the six independent components of the effective stress tensor, i.e. total stress less fluid pressure. The output files from GEOS include effective stress $(\sigma_p - p)$ with tensile stress reckoned positive in the "engineering" sign convention.

DISCUSSION

To validate the modeling, we consider the microseismic events recorded over ten days in December 2016 by a seismic array consisting of 1302 single-component seismographs deployed before, during, and after a planned shutdown in December 2016 (Warren et al., 2018; Warren et al., 2019a; Thurber et al., 2021; Guo et al., 2022). The data set includes precise locations, focal mechanisms, and magnitudes for 106 microseismic events, as described most recently by Guo et al. (2023). As shown in Figure 7, all of these events have coda magnitude less than zero.

We then evaluate the Coulomb failure criterion on sets of planes using the simulated stress field calculated by a GEOS solution. We assume that the rock is critically stressed during normal operations. We make the following assumptions:

Following equation (3) of Oppenheimer et al. (1988), we write the "proximity of a rock volume to failure" as a Coulomb failure function $F = |\tau_p| - \mu(\sigma_p - p) - S_0$,where $|\tau_P|$ is the "magnitude of the shear traction vector", σ_P is the "normal traction (a scalar)" and p is the "fluid pore pressure within the rock". We assume that the "internal friction" coefficient $\mu = 0.6$ and that cohesion $S_0 = 0$. We follow more recent conventions and denote the value of F as *CFS* and temporal changes in F as ΔCFS. Since the magnitude of the shear stress is always positive, *CFS* does not distinguish between dextral and sinistral shear. Similar notational conventions appear elsewhere (e.g., Vavryčuk, 2014; Kusumawati et al., 2021). Oppenheimer et al. (1988) also note that "a physical assumption implicit in the criterion is that the quantity $\sigma_P - p$ [effective stress] be greater than zero; otherwise different modes of failure will occur", citing Jaeger and Cook (1979, p. 96). To follow this sign convention, as used in rock mechanics, we multiply each component of the stress tensor from GEOS by –1.

Here, we consider only the 32 microseismic events for which *Guo et al.* (2023) calculated a focal mechanism from seismic data. Each event includes two possible fault planes specified by their strike, dip, and rake (Figure 8). We evaluate the change ΔCFS in Coulomb failure stress on each plane during each of the time steps during the shutdown in December 2016 in Figure 9. According to the sign convention used in rock mechanics, positive values of ΔCFS indicate conditions favorable to fault slip. The ΔCFS values are calculated with respect to a reference time of 2016/12/08 19:23 UTC, i.e., ten minutes before the shutdown began. The simulated change in Coulomb Failure Stress ΔCFS is positive for 28 of the 32 events (88%) for which focal mechanisms were determined by *Guo et al.* (2023).

This result is fairly sensitive to the permeability values assumed in the modeling. For example, decreasing the permeabilities in the X- and Y directions to 10% of the values increases the number of events for which ΔCFS is positive from 28 to 29 of 32. In the future, we plan to conduct additional such tests of sensitivity.

CONCLUSIONS

Using the GEOS simulation code to account for hydro-mechanical processes over short time scales on the order of hours to days, we have calculated the stress field as a function of time. The simulated change in Coulomb Failure Stress ΔCFS agrees very well with the focal mechanisms determined by Guo et al. (2023).

To perform a post-audit of the model results, we will use data from a seismic array consisting of 450 three-component seismographs deployed before, during, and after a planned shutdown in April 2022 (Feigl et al., 2022a). We plan to compare timing and location of the microseismic events inferred from the seismic data with the timing and location calculated by the GEOS simulations.

ACKNOWLEDGMENTS

The WHOLESCALE team thanks the following individuals at Ormat: Curtis Peach, Cliff Reed, Joe Pavone, Manolo Di Donato, Leeta Miller, Alan Pinuelas-Molina, David Schwab, Lupé Gonsalez Ortiz, Gabrielle Ramirez, Courtney Brailo, John Murphy, and Robin Zuza. We also acknowledge the data shared by Ormat Technologies, Inc.

Some of the figures in this paper were generated using Leapfrog Geothermal Software Leapfrog (Bentley Systems, Incorporated).

Passive seismic data collections were completed at San Emidio in late 2016 by Microseismic Inc. as part of DOE project number DE-EE0007698 as described at https://gdr.openei.org/submissions/1386

The work presented herein has been funded in part by the Office of Energy Efficiency and Renewable Energy (EERE), U.S. Department of Energy, under Award Numbers DE-EE0007698 and DE-EE0009032. Parts of this work were performed under the auspices of the U.S. Department of Energy by Lawrence Livermore National Laboratory under Contract DE-AC52-07NA27344.

REFERENCES

Akerley, J., I. Warren, E. Gasperikova, and S. Pullammanappallil (2023), A Novel Approach to Map Permeability Using Passive Seismic Emission Tomography, United States. https://www.osti.gov/biblio/1986084

Andrés, S., D. Santillán, J. C. Mosquera, and L. Cueto-Felgueroso (2019), Thermo-Poroelastic Analysis of Induced Seismicity at the Basel Enhanced Geothermal System, Sustainability, 11. http://dx.doi.org/10.3390/su11246904

Blacker, T. D., S. J. Owen, M. L. Staten, W. R. Quadros, B. Hanks, B. W. Clark, R. J. Meyers, C. Ernst, K. Merkley, R. Morris, C. McBride, C. J. Stimpson, M. Plooster, and S. Showman (2016), CUBIT geometry and mesh generation toolkit 15.1 user documentation, United States. https://www.osti.gov/biblio/1430472

Brodsky, E. E., and L. J. Lajoie (2013), Anthropogenic Seismicity Rates and Operational Parameters at the Salton Sea Geothermal Field, Science. http://dx.doi.org/10.1126/science.1239213

Cardiff, M., D. D. Lim, J. R. Patterson, J. Akerley, P. Spielman, J. Lopeman, P. Walsh, A. Singh, W. Foxall, H. F. Wang, N. E. Lord, C. H. Thurber, D. Fratta, R. J. Mellors, N. C. Davatzes, and K. L. Feigl (2018), Geothermal production and reduced seismicity: Correlation and proposed mechanism, Earth and Planetary Science Letters, 482, 470-477. https://doi.org/10.1016/j.epsl.2017.11.037

Cardiff, M., C. Sherman, H. Guo, E. Cunningham, M. Folsom, I. Warren, H. Sone, C. Thurber, H. F. Wang, and K. L. Feigl (2023a), WHOLESCALE - Calibration and Simulation of hydro-mechanical Behavior at San Emidio, Nevada During Operational Changes, paper presented at Stanford Geothermal Workshop, Stanford, California. https://pangea.stanford.edu/ERE/db/GeoConf/papers/SGW/2023/Cardiff.pdf

Cardiff, M. A., C. Sherman, H. Guo, X. Luo, J. Akerley, H. Sone, C. H. Thurber, H. F. Wang, and K. L. Feigl (2023b of Conference), Monitoring and Modeling of Pumping-induced Pressure Changes at a Natural Geothermal Reservoir Complex: The WHOLESCALE Project at San Emidio, NV, abstract presented at AGU.

Ellsworth, W. L. (2013), Injection-induced earthquakes, Science, 341, 1225942. http://www.ncbi.nlm.nih.gov/pubmed/23846903

Eneva, M., G. Falorni, W. Teplow, J. Morgan, G. Rhodes, and D. Adams (2011), Surface Deformation at the San Emidio Geothermal Field, Nevada, from Satellite Radar Interferometry, GRC Transactions, 35.

Faulds, J. E. (2014), 3D Model of the San Emidio Geothermal Area [data set], Geothermal Data Repository. https://gdr.openei.org/submissions/365.

Feigl, K., C. Thurber, and N. Lord (2022a), WHOLESCALE survey at San Emidio, Nevada, USA [Data set]. https://doi.org/10.7914/m5qt-mh37

Feigl, K. L., and L. M. Parker (2019), PoroTomo Final Technical Report: Poroelastic Tomography by Adjoint Inverse Modeling of Data from Seismology, Geodesy, and Hydrology, Medium: ED; Size: 176 p. pp, ; Univ. of Wisconsin, Madison, WI (United States). https://www.osti.gov/servlets/purl/1499141

Feigl, K. L., E. C. Reinisch, S. A. Batzli, H. Sone, M. A. Cardiff, J. C. Hampton, N. E. Lord, C. H. Thurber, H. F. Wang, and C. Sherman (2020), Spatio–Temporal Analysis of Deformation at San Emidio Geothermal Field, Nevada, USA between 1992

and 2010, paper presented at Proceedings 45th Workshop on Geothermal Reservoir Engineering Stanford University, Stanford, California, February 10-12, 2020. https://pangea.stanford.edu/ERE/db/GeoConf/papers/SGW/2020/Feigl.pdf

Feigl, K. L., S. Tung, H. Guo, E. Cunningham, J. Hampton, S. J. Kleich, B. Jahnke, B. Heath, C. Roland, M. Folsom, J. Akerley, M. Cusini, C. Sherman, I. Warren, C. Kreemer, H. Sone, M. A. Cardiff, N. E. Lord, C. H. Thurber, and H. F. Wang (2022b), Overview and Preliminary Results from the WHOLESCALE project at San Emidio, Nevada, U.S., paper presented at 47th Workshop on Geothermal Reservoir Engineering, Stanford, California. https://pangea.stanford.edu/ERE/pdf/IGAstandard/SGW/2022/Feigl.pdf

Feigl, K. L., H. Guo, E. Cunningham, J. Hampton, M. Folsom, J. Akerley, M. Cusini, C. Sherman, I. Warren, C. Kreemer, H. Sone, M. A. Cardiff, N. E. Lord, P. E. Sobol, S. A. Batzli, C. H. Thurber, and H. F. Wang (2023), The 2022 WHOLESCALE deployment at San Emidio, Nevada, U.S., paper presented at 48th Workshop on Geothermal Reservoir Engineering, Stanford University, Stanford, California, February 6-8, 2023 SGP-TR-224. https://pangea.stanford.edu/ERE/db/GeoConf/papers/SGW/2023/Feigl.pdf

Folsom, M., R. Libbey, D. Feucht, W. I., and S. Garanzini (2020), Geophysical Observations and Integrated Conceptual Models of the San Emidio Geothermal Field, Nevada., paper presented at Workshop on Geothermal Reservoir Engineering, Stanford, California, USA. https://pangea.stanford.edu/ERE/db/GeoConf/papers/SGW/2020/Folsom.pdf

Folsom, M., R. Libbey, D. Feucht, I. Warren, and S. Garanzini (2021), Geophysical observations and integrated conceptual models of the San Emidio Geothermal Field, Nevada, paper presented at Nevada Petroleum & Geothermal Society, February 4th, 2021.

Guo, H., C. H. Thurber, B. A. Heath, M. Cardiff, N. Lord, I. Warren, and K. L. Feigl (2022 of Conference), Seismic analysis of reservoir conditions for inducing seismicity at the San Emidio geothermal field, Nevada, U.S.A., abstract presented at Annual Meeting Seismological Society of America, Bellevue, WA, USA, 19-23 April 2022.

Guo, H., C. Thurber, I. Warren, B. A. Heath, M. Folsom, H. Sone, N. Lord, J. Akerley, and K. L. Feigl (2023), Enhanced Microseismicity During Production Pumping Cessation at the San Emidio Geothermal Field (Nevada, USA) in December 2016, Journal of Geophysical Research: Solid Earth, 128, e2023JB027008. https://doi.org/10.1029/2023JB027008

Jaeger, J. C., and N. G. W. Cook (1979), Fundamentals of Rock Mechanics, 3rd edition ed., 593 pp., Chapman and Hall, London.

Jahnke, B. (2022), Geomechanical Analysis of the Geothermal Reservoir at San Emidio, Nevada and Fracture Toughness Anisotropy of EGS Collab Testbed Rocks, M.S. thesis thesis, University of Wisconsin-Madison (H. Sone, advisor).

Jahnke, B., H. Guo, B. Heath, E. Cunningham, C. Sherman, H. Sone, I. Warren, C. Kreemer, C. H. Thurber, K. F. Feigl, and WHOLESCALE_Team (2022), Spatial-Temporal Stress Heterogeneity in the Geothermal Reservoir at San Emidio, Nevada, U.S., paper presented at 45th Workshop on Geothermal Reservoir Engineering, February 7-9, 2022, Stanford University, Stanford, California,. https://pangea.stanford.edu/ERE/pdf/IGAstandard/SGW/2022/Jahnke.pdf

Jahnke, B., H. Sone, H. Guo, C. Sherman, I. Warren, C. Kreemer, C. H. Thurber, and K. L. Feigl (2023), Geomechanical analysis of the geothermal reservoir at San Emidio, Nevada, Geothermics, 110, 102683. https://doi.org/10.1016/j.geothermics.2023.102683

Kleich, S. J. (2022), Mechanical and Poroelastic Properties of Lithologic Units Within the San Emidio Geothermal System, Nevada, United States, M.S. thesis, University of Wisconsin-Madison (J. Hampton, advisor).

Kusumawati, D., D. P. Sahara, S. Widiyantoro, A. D. Nugraha, M. Muzli, I. Imran, N. T. Puspito, and Z. Zulfakriza (2021), Fault Instability and Its Relation to Static Coulomb Failure Stress Change in the 2016 Mw 6.5 Pidie Jaya Earthquake, Aceh, Indonesia, Frontiers in Earth Science, 8.

Kwiatek, G., P. Martínez-Garzón, G. Dresen, M. Bohnhoff, H. Sone, and C. Hartline (2015), Effects of long-term fluid injection on induced seismicity parameters and maximum magnitude in northwestern part of The Geysers geothermal field, Journal of Geophysical Research: Solid Earth, 120, 7085-7101. https://agupubs.onlinelibrary.wiley.com/doi/abs/10.1002/2015JB012362

Lord, N. (2016), Seismic Survey 2016 Metadata at San Emidio, Nevada, University of Wisconsin. https://doi.org/10.15121/1872549

Lord, N. E., B. Heath, H. Guo, I. Warren, S. Bradshaw, C. Thurber, and K. L. Feigl (2022), Seismic Survey 2016 data at San Emidio Nevada. https://gdr.openei.org/submissions/1395

Majer, E. L., R. Baria, M. Stark, S. Oates, J. Bommer, B. Smith, and H. Asanuma (2007), Induced seismicity associated with enhanced geothermal systems, Geothermics, 36, 185-222.

Matlick, J. S. (1995), San Emidio Geothermal System, Empire, Nevada: GRC Field Trip ~ October 1995, Mesquite Group, Inc., Fullerton, California. https://data.nbmg.unr.edu/public/Geothermal/GreyLiterature/Matlick_SanEmidioGeoSystem_1995.pdf

McGarr, A., B. Bekins, N. Burkardt, J. Dewey, P. Earle, W. Ellsworth, S. Ge, S. Hickman, A. Holland, E. Majer, J. Rubinstein, and A. Sheehan (2015), Coping with earthquakes induced by fluid injection, Science, 347, 830-831. http://www.sciencemag.org/content/347/6224/830.full.pdf

Moeck, I. (2011), Stress Inversion and 2D fault stress modeling San Emidio: Project Report to PI Teplow, 19 page pp.

NRC (2013), Induced Seismicity Potential in Energy Technologies, National Acad. Press, Washington, D. C.

Oppenheimer, D. H., P. A. Reasenberg, and R. W. Simpson (1988), Fault plane solutions for the 1984 Morgan Hill, California, Earthquake Sequence: Evidence for the state of stress on the Calaveras Fault, Journal of Geophysical Research: Solid Earth, 93, 9007-9026. https://doi.org/10.1029/JB093iB08p09007

Patterson, J. R., M. Cardiff, T. Coleman, H. Wang, K. L. Feigl, J. Akerley, and P. Spielman (2017), Geothermal reservoir characterization using distributed temperature sensing at Brady Geothermal Field, Nevada, The Leading Edge, 36, 1024a1021 - 1024a1027. http://dx.doi.org/10.1190/tle36121024a1.1

Pulliam, R. J., F. Sepulveda, J. S. Thangraj, D. Quiros, J. Queen, M. Queen, and J. Iovenitti (2019), Development of a Novel, Near Real Time Approach To Geothermal Seismic Exploration And Monitoring Via Ambient Seismic Noise Interferometry, Medium: ED pp, Baylor Univ., Waco, TX (United States). https://www.osti.gov/servlets/purl/1648329

Raleigh, C. B., J. H. Healy, and J. D. Bredehoeft (1976), An experiment in earthquake control at rangely, colorado, Science, 191, 1230-1237. http://www.ncbi.nlm.nih.gov/pubmed/17737698

Reinisch, E. C., M. Cardiff, J. Akerley, I. Warren, and K. L. Feigl (2019), Spatio–Temporal Analysis of Deformation at San Emidio Geothermal Field, Nevada, USA Between 1992 and 2010, Remote Sensing, 11, 1935. http://dx.doi.org/10.3390/rs11161935

Rhodes, G. T., J. E. Faulds, and W. Teplow (2010), Structural Controls of the San Emidio Desert Geothermal Field, Northwestern Nevada, paper presented at Geothermal Resource Council Transactions.

Rhodes, G. T. (2011), Structural controls of the San Emidio Geothermal System, M.S. thesis, vi, 73 leaves pp, University of Nevada Reno advisor).

Rhodes, G. T., J. E. Faulds, and A. R. Ramelli (2011), Preliminary Geologic Map of the Northern Lake Range, San Emidio Geothermal Area, Washoe County, Nevada, Nevada Bureau of Mines and Geology. http://data.nbmg.unr.edu/public/freedownloads/of/of2011-11.zip

Segall, P., and S. Lu (2015), Injection-induced seismicity: Poroelastic and earthquake nucleation effects, Journal of Geophysical Research: Solid Earth, 120, 5082-5103. http://dx.doi.org/10.1002/2015jb012060

Settgast, R. R., J. A. White, B. C. Corbett, A. Vargas, C. Sherman, P. Fu, and C. Annavarapu (2018), GEOSX Simulation Framework: General multi-physics simulation framework targeting exascale computing platforms, Medium: X; OS: Any pp., Lawrence Livermore National Lab. (LLNL), Livermore, CA (United States). https://www.osti.gov/biblio/1422506

Sone, H., Z. Jin, O. Mudatsir, I. Warren, M. Folsom, and K. L. Feigl (2023), WHOLESCALE - Characterization of Conductive Fractured Zones Based on Borehole Data at San Emidio Geothermal Field, Nevada, paper presented at Stanford Geothermal Workshop. https://pangea.stanford.edu/ERE/db/GeoConf/papers/SGW/2023/Sone.pdf

Teplow, W. J., and I. Warren (2015), Finding Large Aperture Fractures in Geothermal Resource Areas Using a Three-Component Long-Offset Surface Seismic Survey, PSInSAR and Kinematic Structural Analysis, Medium: ED; Size: 52 p. pp, US Geothermal, Inc., Boise, ID (United States). https://doi.org/10.2172/1213113

Thurber, C. H., H. Guo, B. A. Heath, M. Cardiff, N. Lord, I. Warren, and K. L. Feigl (2021 of Conference), Structure and Stress Results from Nodal Seismic Array Deployments at the San Emidio Geothermal Field, Nevada, U.S.A., abstract presented at AGU Fall Meeting, New Orleans. https://agu.confex.com/agu/fm21/meetingapp.cgi/Paper/912296

Trugman, D. T., P. M. Shearer, A. A. Borsa, and Y. Fialko (2016), A comparison of long-term changes in seismicity at The Geysers, Salton Sea, and Coso geothermal fields, Journal of Geophysical Research: Solid Earth, 121, 225-247. http://dx.doi.org/10.1002/2015jb012510

UNR (2014), Slip and Dilation Tendency Analysis of the San Emidio Geothermal Area [data set]. https://gdr.openei.org/submissions/371

Vavryčuk, V. (2014), Iterative joint inversion for stress and fault orientations from focal mechanisms, Geophysical Journal International, 199, 69-77. https://doi.org/10.1093/gji/ggu224

Warren, I. (2010), Three-Component Long Offset Surface Seismic Survey Data Used to Find Large Aperture Fractures in Geothermal Resources - San Emidio Geothermal Resource Area, U.S. Geothermal Inc. https://doi.org/10.15121/1422726

Warren, I., E. Gasperikova, S. Pullammanappallil, S. Sennert, and M. Grealy (2018), Mapping Geothermal Permeability Using Passive Seismic Emission Tomography Constrained by Cooperative Inversion of Active Seismic and Electromagnetic Data, paper presented at Proceedings, 43rd Workshop on Geothermal Reservoir Engineering Stanford University, Stanford, California, 2018 SGP-TR-213, February 12-14, 2018. https://pangea.stanford.edu/ERE/pdf/IGAstandard/SGW/2018/Warren.pdf

Warren, I., E. Gasperikova, and S. Pullammanappallil (2019a), Final Phase 1 Report DE-EE0007698: A Novel Approach to Map Permeability Using Passive Seismic Emission Tomography. https://subterraseis.com/wp-content/uploads/2019/10/Doc1.pdf

Warren, I., E. Gasperikova, S. Pullammanappallil, S. Sennert, and M. Grealy (2019b), A Novel Approach to Map Permeability Using Passive Seismic Emission Tomography, paper presented at World Geothermal Conference.

FIGURES

# name	unit	fieldName	component	scale
permeability_x_QTA	m^2	rockPerm_permeability	0	1.50E-12
permeability_y_QTA	m^2	rockPerm_permeability	1	1.50E-12
permeability_z_QTA	m^2	rockPerm_permeability	2	1.07E-14
porosity_QTA		rockPorosity_referencePorosity	NA	3.00E-01
permeability_x_QAS	m^2	rockPerm_permeability	0	4.30E-11
permeability_y_QAS	m^2	rockPerm_permeability	1	4.30E-11
permeability_z_QAS	m^2	rockPerm_permeability	2	3.07E-13
porosity_QAS		rockPorosity_referencePorosity	NA	3.50E-01
permeability_x_TPTS	m^2	rockPerm_permeability	0	1.70E-12
permeability_y_TPTS	m^2	rockPerm_permeability	1	1.70E-12
permeability_z_TPTS	m^2	rockPerm_permeability	2	1.70E-12
porosity_TPTS		rockPorosity_referencePorosity	NA	5.00E-02
permeability_x_TPTSPRIME	m^2	rockPerm_permeability	0	2.40E-11
permeability_y_TPTSPRIME	m^2	rockPerm_permeability	1	2.40E-11
permeability_z_TPTSPRIME	m^2	rockPerm_permeability	2	2.40E-11
porosity_TPTSPRIME		rockPorosity_referencePorosity	NA	1.00E-01
permeability_x_TRJN	m^2	rockPerm_permeability	0	3.10E-14
permeability_y_TRJN	m^2	rockPerm_permeability	1	3.10E-14
permeability_z_TRJN	m^2	rockPerm_permeability	2	3.10E-14
porosity_TRJN		rockPorosity_referencePorosity	NA	5.00E-02
permeability_x_TS	m^2	rockPerm_permeability	0	3.10E-14
permeability_y_TS	m^2	rockPerm_permeability	1	3.10E-14
permeability_z_TS	m^2	rockPerm_permeability	2	3.10E-14
bulk_modulus_QTA	Pa	rock_bulkModulus	NA	7.40E+09
shear_modulus_QTA	Pa	rock_shearModulus	NA	4.50E+09
density_QTA	kg/m^3	rock_density	NA	2.12E+03
bulk_modulus_QAS	Pa	rock_bulkModulus	NA	5.70E+09
shear_modulus_QAS	Pa	rock_shearModulus	NA	4.30E+09
density_QAS	kg/m^3	rock_density	NA	2.40E+03
bulk_modulus_TPTS	Pa	rock_bulkModulus	NA	1.55E+10
shear_modulus_TPTS	Pa	rock_shearModulus	NA	1.26E+10
density_TPTS	kg/m^3	rock_density	NA	2.12E+03
bulk_modulus_TPTSPRIME	Pa	rock_bulkModulus	NA	1.74E+10
shear_modulus_TPTSPRIME	Pa	rock_shearModulus	NA	1.41E+10
density_TPTSPRIME	kg/m^3	rock_density	NA	2.67E+03
bulk_modulus_TRJN	Pa	rock_bulkModulus	NA	2.04E+10
shear_modulus_TRJN	Pa	rock_shearModulus	NA	1.66E+10
density_TRJN	kg/m^3	rock_density	NA	2.67E+03
bulk_modulus_TS	Pa	rock_bulkModulus	NA	2.86E+10
shear_modulus_TS	Pa	rock_shearModulus	NA	2.15E+10
density_TS	kg/m^3	rock_density	NA	2.80E+03
biot_QTA		rockPorosity_biotCoefficient	NA	3.60E-01
biot_QAS		rockPorosity_biotCoefficient	NA	3.60E-01
biot_TPTS		rockPorosity_biotCoefficient	NA	3.60E-01
biot_TPTSPRIME		rockPorosity_biotCoefficient	NA	3.60E-01
biot_TRJN		rockPorosity_biotCoefficient	NA	3.60E-01
biot_TS		rockPorosity_biotCoefficient	NA	3.60E-01
fault_se_permeability_x	m^2	rockPerm_permeability	0	1.50E-12
fault_se_permeability_y	m^2	rockPerm_permeability	1	1.50E-12
fault_se_permeability_z	m^2	rockPerm_permeability	2	1.07E-14
porosity_TS		rockPorosity_referencePorosity	NA	5.00E-02

Figure 1. Material properties for each set of elements.

# name	fieldName	component	setNames	scale	functionName
xconstraint	totalDisplacement	0	xneg;xpos;yneg;ypos	0	NA
yconstraint	totalDisplacement	1	xneg;xpos;yneg;ypos	0	NA
zconstraint	totalDisplacement	2	zneg	0	NA
edge_pressure	pressure	NA	yneg;ypos	1	edge_pressure
well_25A_21	NA	NA	well_25A_21	987	well_25A_21
well_75B_16	NA	NA	well_75B_16	926	well_75B_16
well_76_16	NA	NA	well_76_16	931	well_76_16
well_42_21	NA	NA	well_42_21	-987	well_42_21
well_43_21	NA	NA	well_43_21	-987	well_43_21
well_53_21	NA	NA	well_53_21	-987	well_53_21
well_61_21	NA	NA	well_61_21	923	well_61_21

Figure 2. Boundary conditions for hydrologic and mechanical processes.

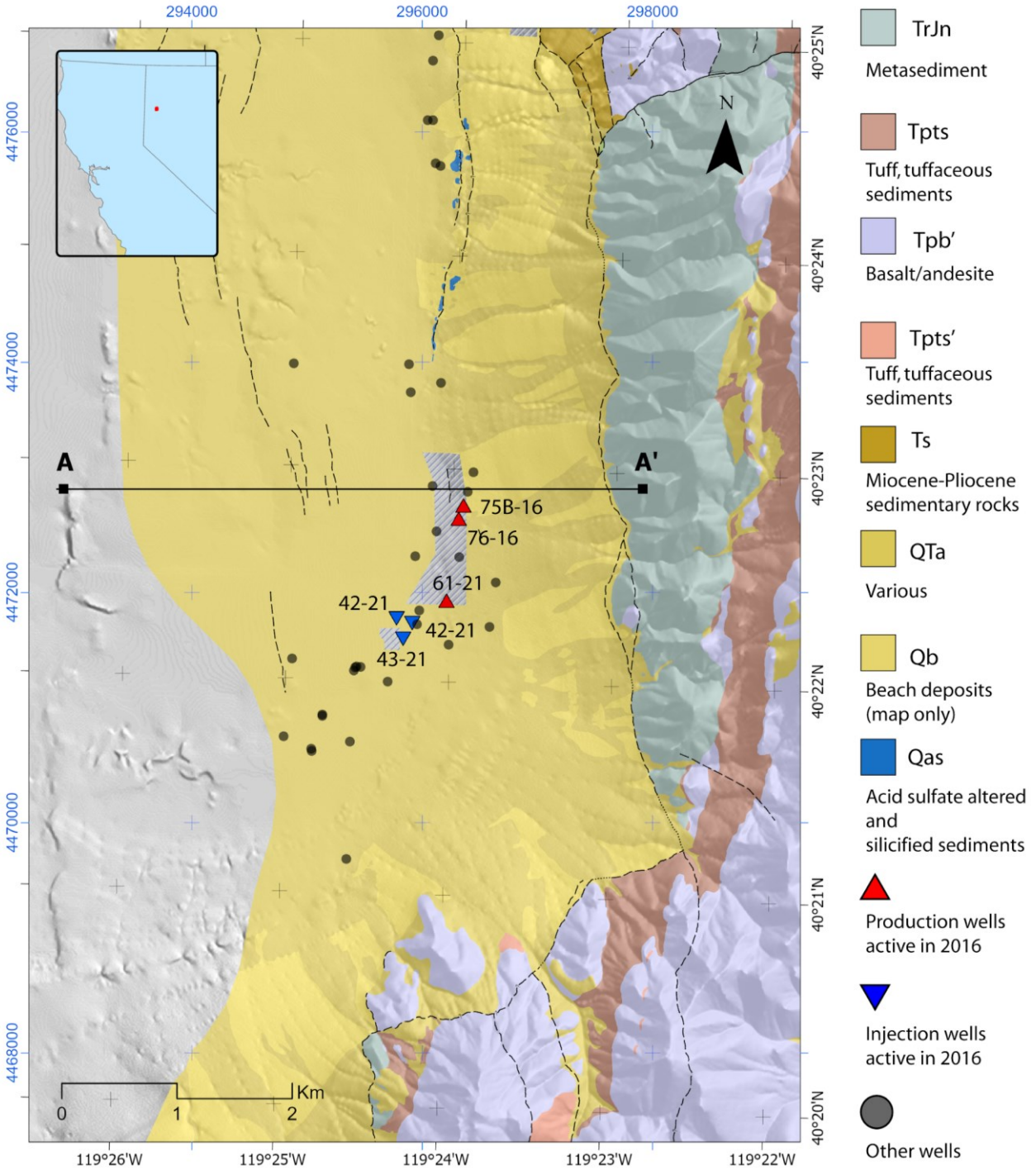

Figure 3. Map of the WHOLESCALE study area at San Emidio, showing geologic model simplified from mapping [*Rhodes FauldsRamelli*, 2011]. Black tick marks and labels on the east and south edges give geographic (WGS84) latitude and longitude, respectively in degrees and minutes. Blue ticks and labels on north and west edges give easting and northing coordinates, respectively, in meters in Zone 11 of the Universal Transverse Mercator (UTM) projection.

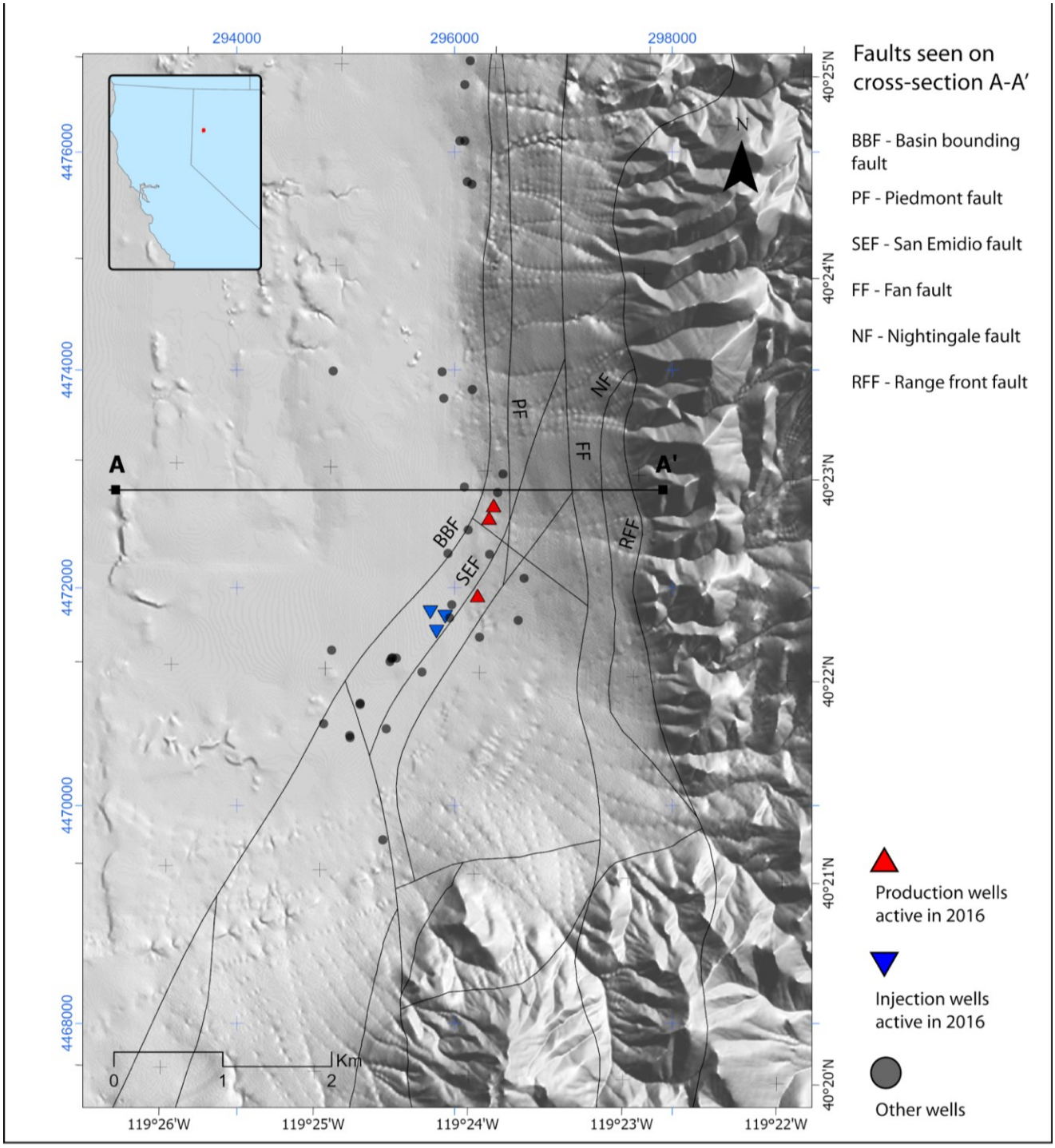

Figure 4. Map of the WHOLESCALE study area at San Emidio, showing surface traces of faults in a geologic model updated by Matt Folsom in 2022. Faults include: Basin-bounding fault (BBF), San Emidio Fault (SRF), Piedmont Fault (PF), Nightingale Fault (NF), and Range Front Fault (RFF). Black tick marks and labels on the east and south edges give geographic (WGS84) latitude and longitude, respectively in degrees and minutes. Blue ticks and labels on north and west edges give easting and northing coordinates, respectively, in meters in Zone 11 of the Universal Transverse Mercator (UTM) projection.

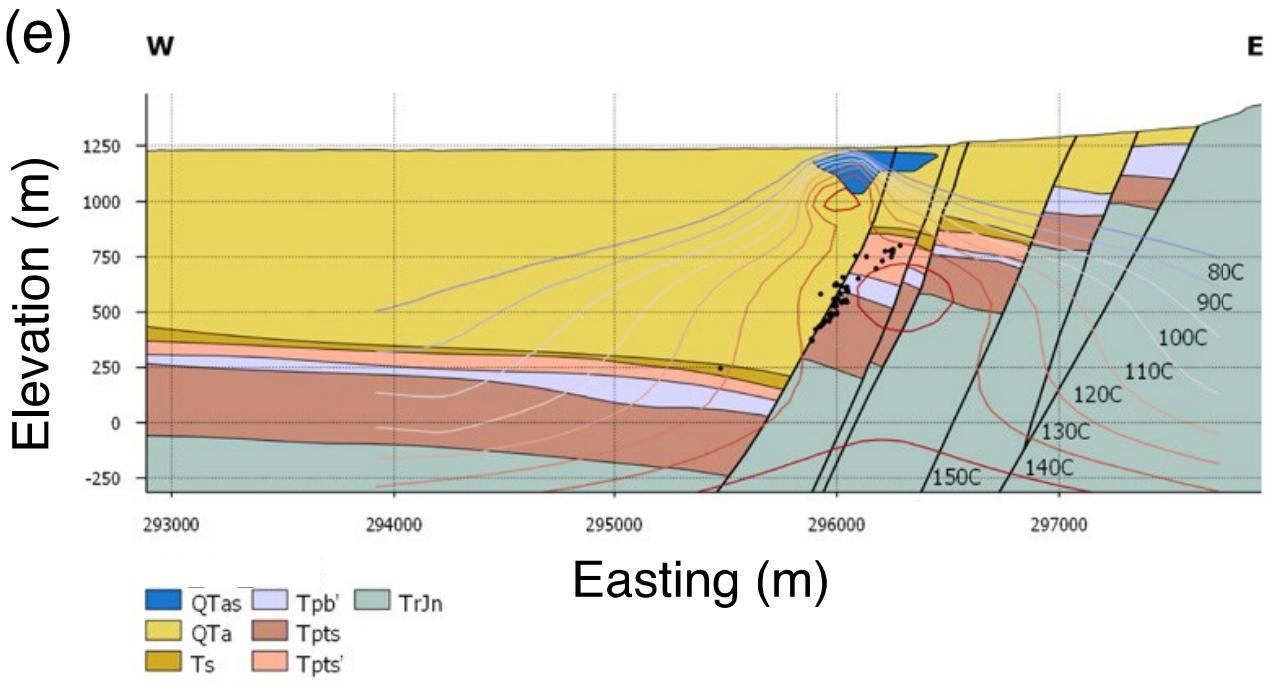

Figure 5. Geologic cross section, showing primary lithologic units, wells, and faults, as updated in 2022 with geologic units consistent with those mapped in the field (Rhodes et al., 2010; Rhodes, 2011; Rhodes et al., 2011). Color codes denote geologic units: QTas, silicified sediments; QTa, alluvium further subdivided by grain size and clay content; Ts, Late Miocene siltstones, tilted and indurated; Tpb', Upper basaltic andesite; Tpts, Lower tuffs; Tpts', Upper tuffs and tuffaceous sediments; TrJn, Nightingale formation. Vertical plane is an E-W transect at UTM Northing coordinate 472,900 m between points A and A' shown in map view (Figure 4). Red contour lines show the "natural state" temperature ranging from 80 °C to 150°C. Faults (black lines) and relocated microseismic events (black dots) have been projected from 200 m onto the vertical plane. Most of the hypocenters are located between the San Emidio Fault (SEF) and the Basin Bounding Fault (BBF). Horizontal axis shows Easting coordinate in meters. Vertical coordinate axis shows elevation above mean sea level (WGS 84 geoid) in meters. (Guo et al., 2023).

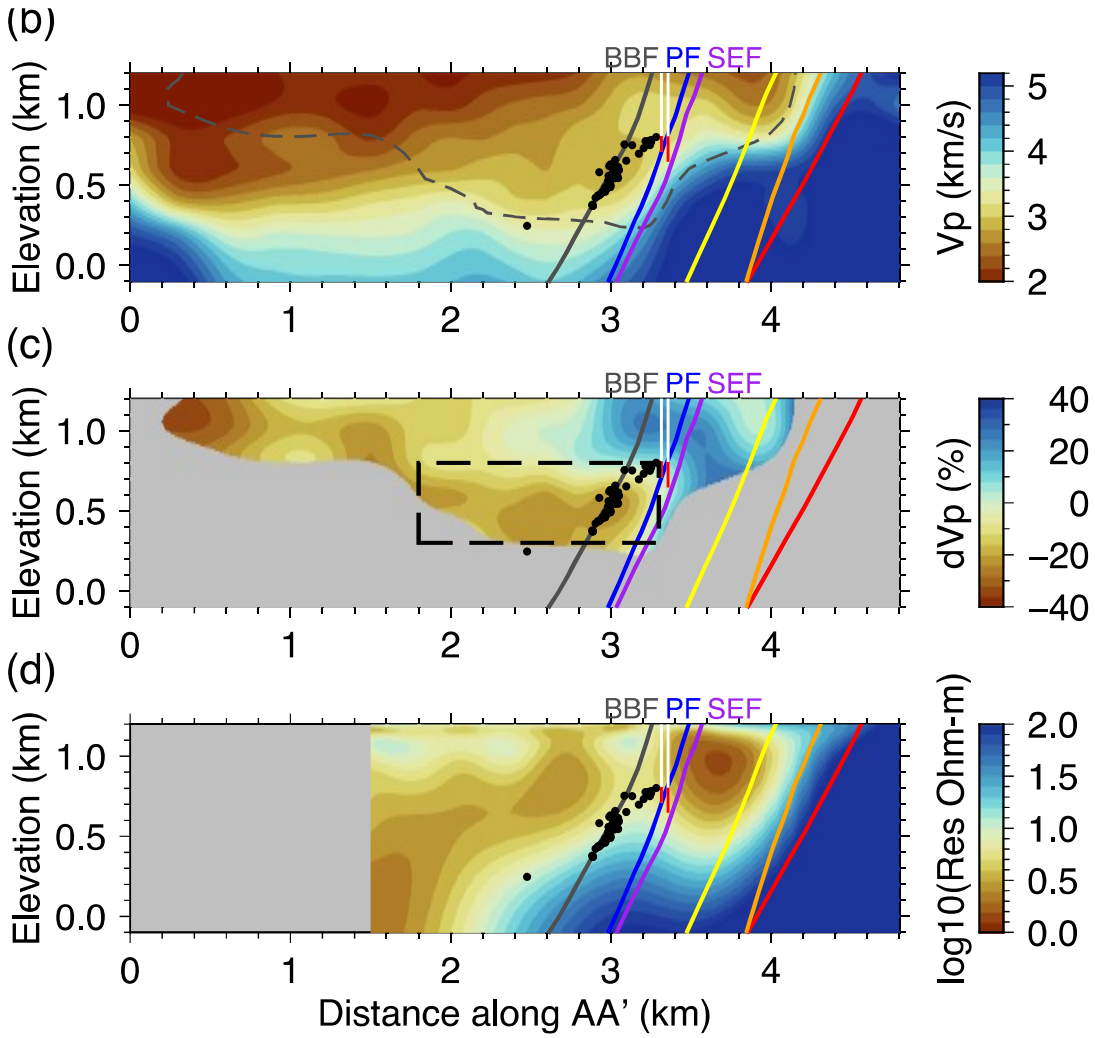

Figure 6. Vertical cross sections showing P-wave velocity from seismic tomography (b, c) and resistivity (d). Panel (b) shows the P-wave velocity in km/s. The dashed gray lines represent the model resolvability contour of 0.7, estimated from a checkerboard resolution test. Panel (c) shows the P-wave velocity perturbation in percentage relative to the 1-D depth-averaged model. The low-resolution regions are masked. Panel (d) shows the resistivity model from Folsom et al. (2020). The region where there is no MT station at the surface is cut. Resistivity values range from 1 Ω·m (red) to 100 Ω·m (blue). In each panel, the black dots show hypocenters of microseismic events (Guo et al., 2023) located within 200 m of the cross-section. The depth trajectories of wells 75B-16 and 76-16 (white-to-red lines with the red segments representing the perforated sections) and fault traces at depth (colored dipping lines) are projected onto the cross section. Figure and caption (Guo et al., 2023).

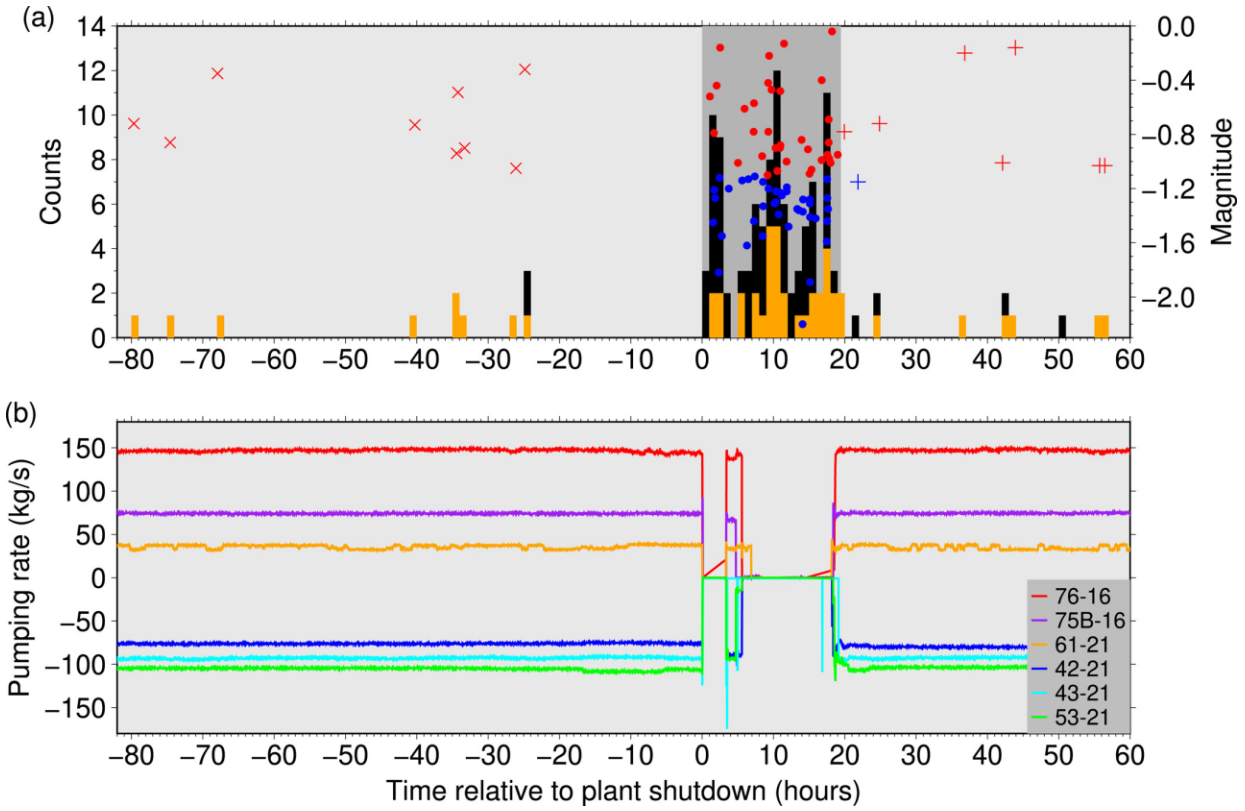

Figure 7. Temporal evolution of seismicity and pumping rates of production and injection. (a) Seismicity. The plant shutdown period (t = 0–19.45 hr) is shaded. The plant shutdown began at 2016-12-08 19:33 UTC. The number of MSEs per hour is shown as black and orange bars with the vertical axis shown on the left. The black bars are for all the events in the catalog. The orange bars are for the relocated events above magnitude −1.1. Note that some black bars are completely covered by orange bars. Crosses, dots, and pluses show magnitudes (vertical axis on the right) of the relocated events before shutdown, during shutdown, and after restart, respectively. These symbols are colored in red and blue for the events above and below magnitude −1.1, respectively. (b) Pumping rate (positive, production; negative, injection). The red, purple, and orange lines show the pumping rate evolution for the three production wells. The blue, cyan, and green lines are for the three injection wells. There is no pumping at all the wells during shutdown except for a short resumption within the 3–6 hr time window. Figure and caption (Guo et al., 2023).

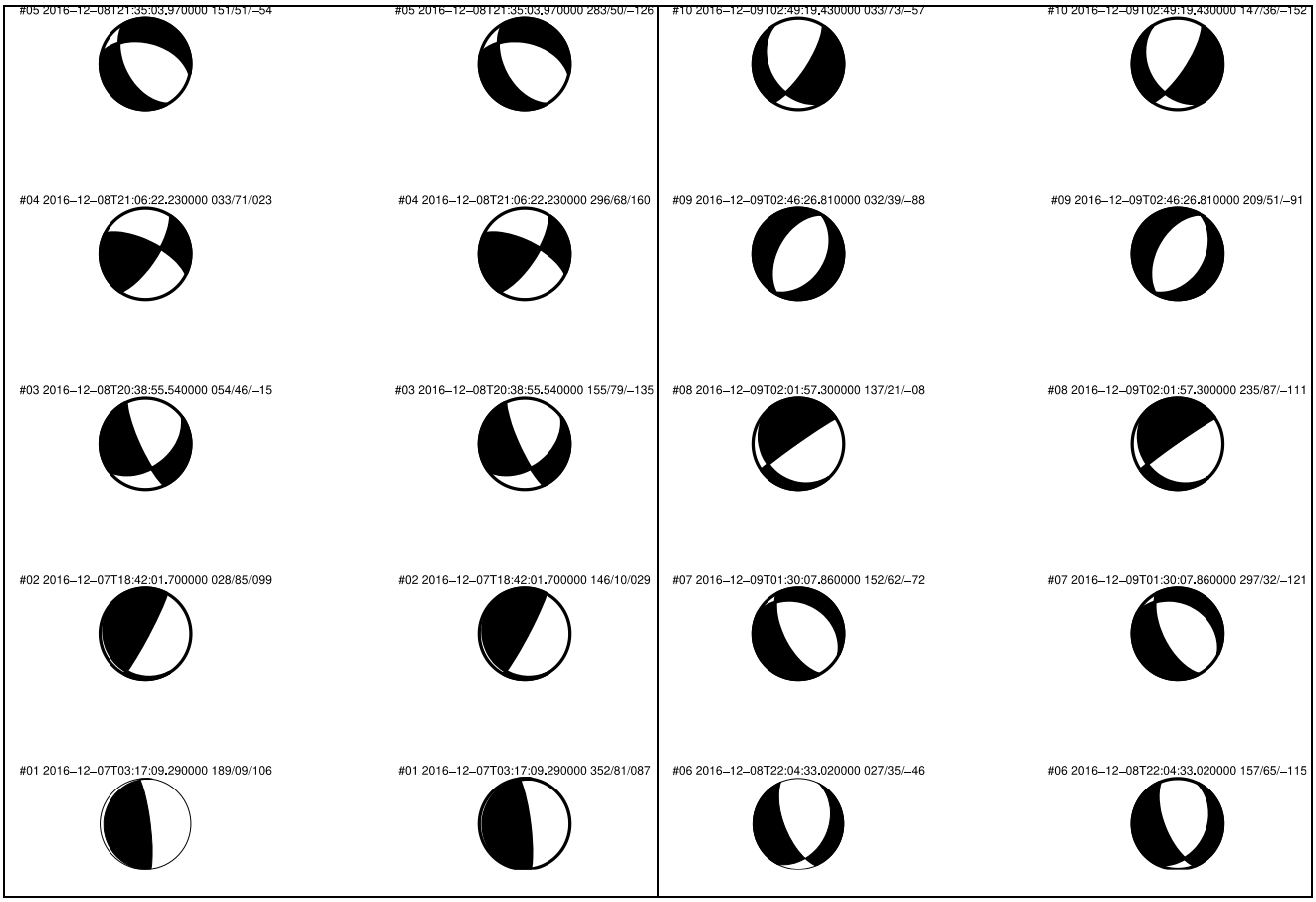

Figure 8. Fault plane solutions for microseismic events in December 2016 listing time of event as well as strike/dip/rake for each of the two possible fault planes (Guo et al., 2023)

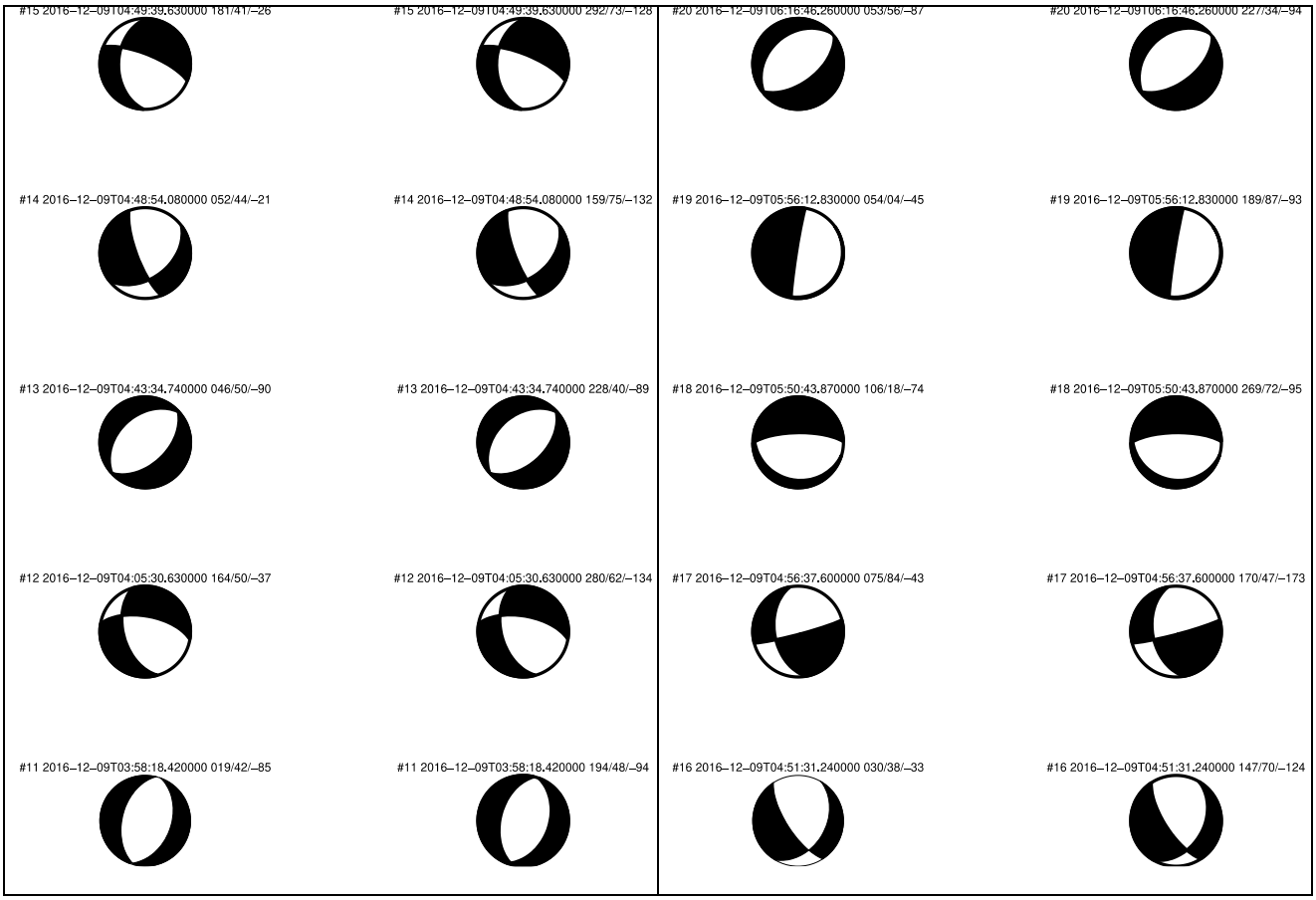

Continuation of previous figure, showing fault plane solutions for microseismic events in December 2016 listing time of event as well as strike/dip/rake for each of the two possible fault planes (Guo et al., 2023).

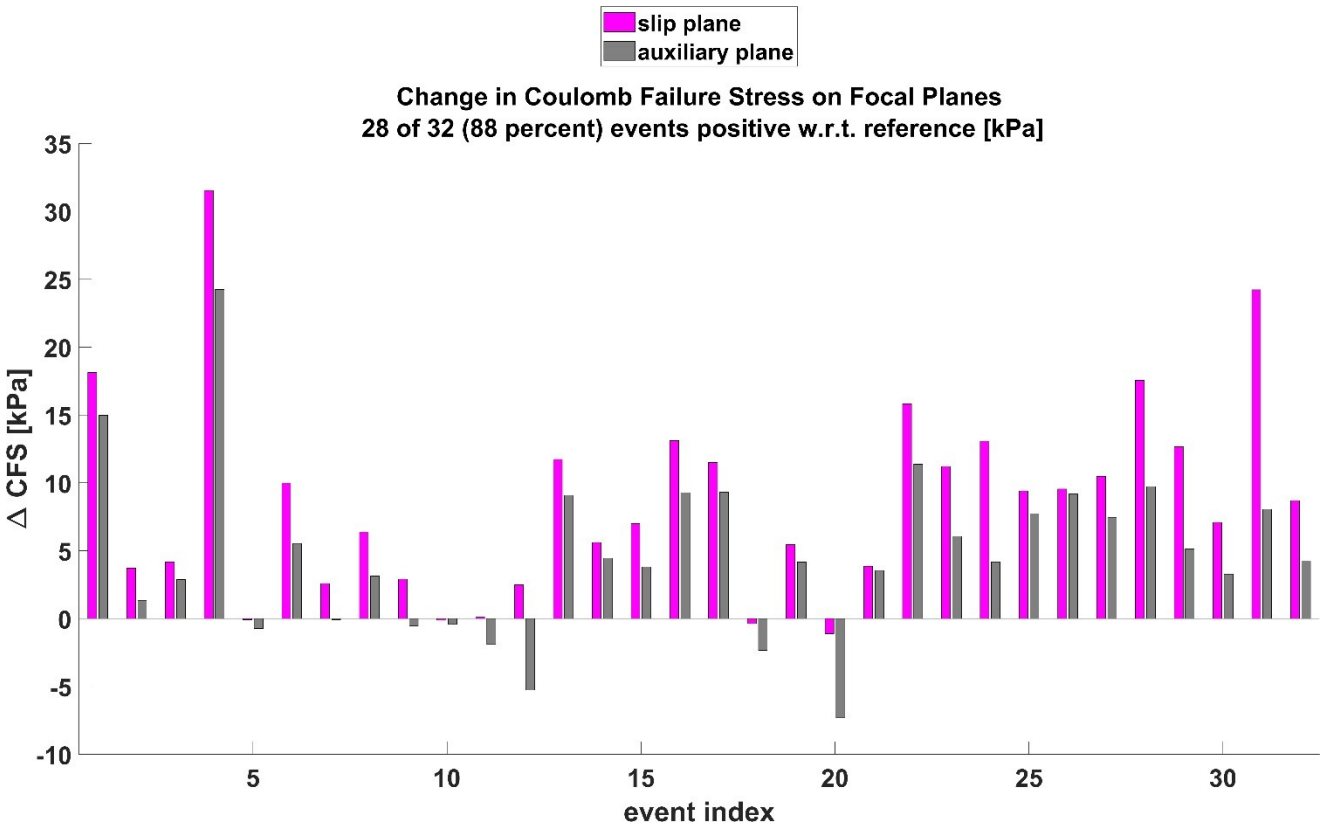

Figure 9. Modeled change in Coulomb Failure Stress (ΔCFS) calculated on fault planes inferred from seismic data. For each event, the magenta bar corresponds to ΔCFS in kPa to the fault plane, the gray bar to the auxiliary plane. According to the sign convention used in rock mechanics, positive values of ΔCFS indicate conditions favorable to fault slip. The ΔCFS values are calculated with respect to a reference time of 2016/12/08 19:23 UTC, i.e., ten minutes before the shutdown began.